Earth Planets Space, **59**, 65–74, 2007

Dynamical modeling of trench retreat driven by the slab interaction with the mantle transition zone

Michio Tagawa, Tomoeki Nakakuki, and Fumiko Tajima

Department of Earth and Planetary Systems Science, Graduate School of Science, Hiroshima University, 1-3-1 Kagami-yama, Higashi-Hiroshima, 739-8526, Japan

(Received April 14, 2006; Revised September 4, 2006; Accepted October 2, 2006; Online published March 21, 2007)

We present the 2-D self-consistent dynamical model of interactions of a subducting slab with the 410-km and 660-km phase boundaries to further our understanding of the relation between the slab stagnation/penetration and the trench migration. Our model takes into account freely-movable plate boundaries and the difference between tensional and compressional yield strengths in the lithosphere. For the case in which the tensional strength is weaker than the compressional one, the negative buoyancy of the subducting slab produces extension of the overriding lithosphere and, accordingly, the trench retreats. Interactions with the 410-km and 660-km phase-transition boundaries further promote the trench retreat, and the dip angle of the slab is substantially decreased. This enhances the resistance of the 660-km phase boundary against the slab penetration. Slab weakening caused by the grain-size reduction in the transition zone may result in a horizontally-lying slab and trench retreat.
Key words: Subduction, tensional strength, trench retreat, grain-size reduction.

1. Introduction

Seismic tomography models visualize variable images of subducted slabs (e.g., van der Hilst *et al*., 1991; Fukao *et al*., 1992; van der Hilst, 1995; Fukao *et al*., 2001); some stagnate horizontally in the mantle transition zone and others penetrate into the lower mantle through the 660-km seismic discontinuity. It is suggested that slab deformation above the 660-km discontinuity is often accompanied by trench retreat, i.e., backward migration of the slab (van der Hilst and Seno, 1993). Tajima and Grand (1998) propose a relationship between trench retreat and a stagnant slab in the northwest Pacific. The 660-km seismic discontinuity is thought to be a phase-transition boundary with a negative Clapeyron slope which acts as a barrier for subduction of a cold slab (e.g., Turcotte and Schubert, 1982; Christensen and Yuen, 1984). On the other hand, Heuret and Lallemand (2005) summarized the tectonics of back-arc spreading and showed a relationship between the dynamics of the subducted slab and the overriding plate. Rollback of a gravitationally unstable slab (e.g., Molnar and Atwater, 1978; Garfunkel *et al*., 1986) is still an important candidate of the mechanism.

The relationship between trench retreat and slab deformation has been studied in laboratory experiments with a chemical boundary (e.g., Kincaid and Olson, 1987; Funiciello *et al*., 2003). Christensen (1996) and Čížková *et al*. (2002) employed kinematic models in their numerical studies. To investigate the effects of the trench migration on the slab interaction with the transition zone, they imposed a priori velocities on the trench migration and the subducting plate. Zhong and Gurnis (1995) concentrated their efforts on constructing dynamical plate models of mantle convection with a rigid overriding plate motion. The resulting trench migration was produced dynamically by rollback of the slab interacting with the 660-km phase boundary. Enns *et al*. (2005) studied the effects of viscosity stratification on slab migration under the condition of no overriding plate. However, back-arc extension driven by dynamical plate motions has not been reproduced in previous numerical models. Therefore, the dynamical relationship between the slab stagnation with slab rollback and the generation of the back-arc basins has not been well understood.

In this study we construct 2-D dynamical models of subduction to understand the roles of slab gravitational instability due to the interaction with the transition zone in the back-arc extension. In our model, the plate motion is generated self-consistently without imposed velocity in the mantle convection system of asymmetric subduction driven by the internal buoyancy. We model subduction at the movable plate boundary under a deformable overriding plate connected to a fixed continent. As a possible mechanism to produce extension of the overriding plate, we consider a tensional yield strength of the lithosphere that is lower than compressional yield strength (e.g., Brace and Kohlstedt, 1980; Kirby, 1980; Scholz, 1990). We also take into account the rheological condition of grain-size reduction (e.g., Rubie, 1984; Riedel and Karato, 1997; Yamazaki *et al*., 2005) after phase transitions in a cold temperature anomaly to induce the slab weakening and deformation in the transition zone. We examine how slab rollback is generated and affects the dynamics of the subducting and overriding plates when the slab subducts and interacts with the transition zone.

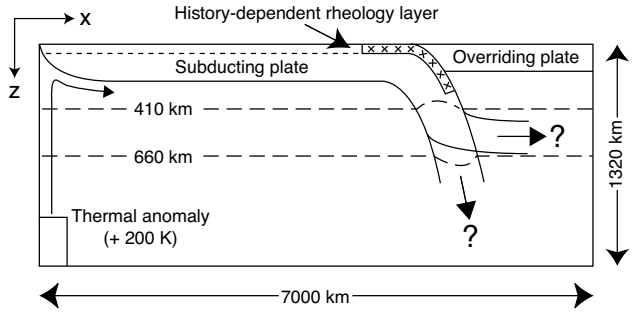

Fig. 1. Schematic illustration of the model. See the text for detail.

Table 1. Parameters used in this study.

c	Friction coefficient	0.3
c_F	Friction coefficient of the fractured segment	0.004
c_p	Specific heat	1.2×10^3 J K^{-1} kg^{-1}
E^*	Activation energy	2.4×10^5 J mol^{-1}
g	Gravity acceleration	10 m s^{-2}
H	Internal heating	5.08×10^{-12} W kg^{-1}
k	Thermal conductivity	4.68 W m^{-1} K^{-1}
m	Grain-size exponent	2
R	Gas constant	8.31451 J mol^{-1} K^{-1}
T_s	surface temperature	273 K
V^*	Activation volume	0.5×10^{-5} m^3 mol^{-1}
α	Thermal expansivity	3.0×10^{-5} K^{-1}
γ_{410}	Clapeyron slope (410 km)	+3.0 MPa K^{-1}
γ_{660}	Clapeyron slope (660 km)	−3.0 MPa K^{-1}
ρ_0	Reference density	3.9×10^3 kg m^{-3}
$\Delta\rho_{410}$	Density contrast (410 km)	323.7 kg m^{-3}
$\Delta\rho_{660}$	Density contrast (660 km)	304.2 kg m^{-3}
τ_f	Cohesive strength of the fractured segment	1 MPa
τ_y	Cohesive strength	10 MPa
τ_{max}	Yield strength of the brittle-ductile transition layer	400 MPa

2. Model Setting and Basic Equations

2.1 Model setup

The subducted slab interacts with the mantle transition zone. We trace the evolution of plate subduction under a deformable overriding plate. We employ a 2-D internally-heated viscous fluid with 7000×1320 km in a Cartesian coordinate and apply an extended Boussinesq approximation (e.g., Christensen and Yuen, 1985). The viscous dissipation and the adiabatic temperature gradient are included in the numerical calculations. Figure 1 shows a schematic view of the model configuration. The top thermal boundary layer consists of two "oceanic" plates that do not contain a buoyant crust; one of these behaves as a subducting plate and the other behaves as an overriding plate. The side boundaries are treated as reflective (i.e., impermeable), tangential stress-free, and thermally insulating. The right-hand sidewall plays the role of an immobile continental plate. The top boundary is set to allow free slip so that the motions of the lithospheres are determined self-consistently by the internal buoyancy. A constant temperature (273 K) is given to the top thermal condition. The bottom boundary is set to be free slip and no heat flux. A thermal anomaly area (+200 K, width = 50 km, height = 400 km) is set at the bottom-left corner as a source of the mantle flow. We assume that the temperature of the lithosphere in the initial condition is determined from a cooling half-space model. The position of the initial plate boundary is set at 4500 km from the left-hand side boundary. The age of the left-hand side plate varies from 0 Ma at $x = 0$ km to 100 Ma at $x = 4500$ km. The right-hand side plate has a uniform thickness with 20 Ma or 100 Ma. The underlying mantle has the adiabatic temperature profile with a potential temperature of 1553 K.

The transition zone is modeled with two phase transitions of olivine-series minerals: olivine to wadsleyite at a depth of 410 km, and ringwoodite to perovskite and magnesiowüstite at a depth of 660 km. The Clapeyron slopes for the 410-km and 660-km phase transitions are assumed to be +3 MPa K^{-1} and −3 MPa K^{-1} (Akaogi *et al.*, 1989; Katsura and Ito, 1989; Akaogi and Ito, 1993), respectively. Although recent high-pressure experiments indicate gentler Clapeyron slopes for the 660-km phase transition (Katsura *et al.*, 2003; Fei *et al.*, 2004), the negative Clapeyron slope employed in this study is consistent with seismological studies of the 660-km discontinuity depression (e.g., Tajima and Grand, 1995; Flanagan and Shearer, 1998; Tajima and Grand, 1998; Tonegawa *et al.*, 2005). The density contrasts for the 410-km and 660-km phase transitions are set to be 8.3% and 7.8%, respectively, based on the PREM model (Dziewonski and Anderson, 1981). Physical parameters are shown in Table 1.

2.2 Rheology

The lithosphere consists of three rheological segments (Kohlstedt *et al.*, 1995), which are the brittle, brittle-ductile transition, and ductile layers. Fractures and rapid deformation of the brittle and brittle-ductile transition layers are expressed by yielding. In this study, stress values, including the yield strength, are described by the definition ($\boldsymbol{\tau} = 2\eta\,\dot{\boldsymbol{\varepsilon}}$), which is usually employed in the fluid dynamics. Note that the differential stress, which is often used to describe the lithospheric strength, is simply twice the stress value in a viscous fluid. The yield strength (τ_Y) of the brittle layer is determined by a Byerlee's law $\tau_Y = \tau_y + c\,p_h$, where τ_y (= 10 MPa) is the cohesive strength, c (= 0.3) the friction coefficient, and p_h is the hydrostatic pressure. The friction coefficient and the cohesive strength used in this study are small compared to that estimated by Byerlee (1978). Because the friction coefficient changes the strength of the shallower part of the lithosphere, the total lithospheric strength changes less than 20%. The cohesive strength (on the order of 10 MPa) is much lower than the yield strength of the lithosphere interior (on the order of 100 MPa). The change in these values does not affect our subduction modeling. The yield strength of the brittle-ductile transition layer is set to be constant τ_{max} (= 400 MPa), which is in the range estimated from the experimental study (Kohlstedt *et al.*, 1995). The strength under tensional stress to generate a normal fault is lower than that under compressional stress to generate a thrust fault (e.g., Brace and Kohlstedt, 1980; Kirby, 1980; Scholz, 1990). We introduce this as a possible mechanism to generate extension of

the lithosphere. For simplicity purposes, the difference between tensional and compressional strengths is modeled by switching the values of c and τ_y depending on the condition of the deviatric horizontal normal stress (τ_{xx}). A ratio ($R_{t/c}$) of tensional strength to compressional strength is defined. If $R_{t/c}$ is 1, the magnitude of the tensional strength is equal to the compressional strength; or if it is 1/3, the tensional strength is weaker than the compressional strength. When the plate is under the tensional stress ($\tau_{xx} > 0$), the tensional strength is set to be $R_{t/c}$ ($\tau_y + c\, p_h$).

Under the stress lower than τ_Y, the viscosity (η_N) is treated as Newtonian with Arrhenius-type temperature (T) and depth (p_h) dependence (e.g., Karato and Wu, 1993), as

$$\eta_N(T, p_h) = \min\left[A_0 \exp\left(\frac{E^* + p_h V^*}{RT}\right),\ \eta_0\right], \quad (1)$$

where A_0 is a constant, E^* the activation energy, V^* the activation volume, and R is the gas constant. A_0 is determined for η_N to have the reference viscosity η_R ($= 5 \times 10^{20}$ Pa·s), which is set to be the average viscosity of the upper mantle (Milne *et al.*, 1999; Okuno and Nakada, 2001), at a depth of 410 km with the initial temperature. η_N is truncated at the maximum η_0 ($= 3 \times 10^{24}$ Pa·s) to simulate the effective viscosity of the plate (Gordon, 2000). This is for the accuracy of numerical calculation. The values of E^* and V^* are based on Karato and Wu (1993).

We introduce grain-size reduction associated with the phase transitions in the cold slab (e.g., Rubie, 1984; Riedel and Karato, 1997; Yamazaki *et al.*, 2005). In this case, the viscosity law depends on the grain size (d), assuming the diffusion creep as

$$\eta_{dif} = \left(\frac{d}{d_0}\right)^m \eta_N(T, p_h), \quad (2)$$

where d_0 is the grain size of the material before a phase transition and m ($= 2$) is the exponent. The grain size is described as a linearized Arrhenius law (Čížková *et al.*, 2002),

$$\begin{aligned} d &= d_{min};\ \text{at } T \le T_{min}, \\ \ln\left(\frac{d}{d_0}\right) &= \frac{T - T_0}{T_0 - T_{min}} \ln\left(\frac{d_0}{d_{min}}\right);\\ &\qquad \text{at } T_{min} < T < T_0, \\ \frac{d}{d_0} &= 1;\ \text{at } T \ge T_0, \end{aligned} \quad (3)$$

where d_{min} is the minimum grain size at T lower than the minimum temperature T_{min} ($= 773$ K). The grain-size reduction (Eq. (3)) progresses in the temperature range between T_{min} and T_0 as the growth in grain size is slower under decreasing temperature. In this temperature range, the viscosity of the slab decreases because of the grain-size reduction. The viscosity becomes lower with decreasing temperature. Here, d_0/d_{min} is assumed to be 10^2 or 10^4. For the maximum temperature T_0 in the region where the grain-size reduction occurs, we test two values: 1073 K or 1873 K. In the case without the grain-size dependence, η_{dif} is set to be η_N.

The effective viscosity (η) depending on the stress is described as

$$\eta = \eta_{dif}\ (\tau_{II} < \tau_Y), \quad (4)$$

$$\eta = \frac{\tau_Y}{2\dot{\varepsilon}_{II}}\ (\tau_{II} = \tau_Y), \quad (5)$$

where τ_{II} and $\dot{\varepsilon}_{II}$ are the second invariants of the deviatric stress tensor (τ_{ij}) and the strain rate tensor ($\dot{\varepsilon}_{ij}$), respectively, and given by

$$\tau_{II} = \sqrt{\frac{1}{2}\sum_{i,j=1}^{2} \tau_{ij}^2}, \quad (6)$$

$$\dot{\varepsilon}_{II} = \sqrt{\frac{1}{2}\sum_{i,j=1}^{2} \dot{\varepsilon}_{ij}^2}. \quad (7)$$

The plate boundary is generated by a layer with history-dependent rheology (Fig. 1) simulating lubrication by an wet oceanic crust. The history-dependent rheology layer which moves with the flow behaves like a passive marker. The thickness of this layer is set to be 20 km to maintain stable plate subduction. Once this layer fractures, the yield strength drops to a smaller value ($\tau_F = \tau_f + c_F p_h$) until healing. Here, τ_f ($= 1$ MPa) is the cohesive strength and c_F ($= 0.004$) is the friction coefficient of the fault zone. The value of c_F is estimated from the ratio between "ridge push" and "continent resistance" (Forsyth and Uyeda, 1975). Note that the strength of this layer is determined by the history of yielding. The segment that has the history-dependent rheology is set in the initial condition. The strength (τ_F) of the plate boundary is assumed to be weaker than that of the bulk of the lithosphere in the initial condition. As the yield strength at the spreading center is assumed to be low because of partial melting (Sleep, 2000), it is also set to be τ_F.

2.3 Basic equations

Basic equations are the equations of continuity, motion, and energy. Using a stream function (ψ), the equation of motion is described as

$$\left(\frac{\partial^2}{\partial x^2} - \frac{\partial^2}{\partial z^2}\right)\left\{\eta\left(\frac{\partial^2\psi}{\partial x^2} - \frac{\partial^2\psi}{\partial z^2}\right)\right\} + 4\frac{\partial^2}{\partial x \partial z}\left(\eta\frac{\partial^2\psi}{\partial x \partial z}\right) = \frac{\partial \rho}{\partial x} g, \quad (8)$$

where x is the horizontal coordinate, z the vertical coordinate, ρ the density, and g is the gravity acceleration. ψ is defined by

$$\boldsymbol{v} = (u, w) \equiv \left(\frac{\partial\psi}{\partial z}, -\frac{\partial\psi}{\partial x}\right), \quad (9)$$

here (u, w) are the x- and z-components of the velocity vector $\boldsymbol{v}$. The equation of continuity is automatically satisfied by the definition of the stream function. The vertical axis is positive in the downward direction. The equation of state provides the density as

$$\rho = \rho_0(1 - \alpha T) + \Delta\rho_{410}\Gamma_{410} + \Delta\rho_{660}\Gamma_{660}, \quad (10)$$

Table 2. Summary of cases.

Case	Phase transitions	$R_{t/c}$	T_0 (K)	d_0/d_{min}	t_p (Ma)	Initial model
1	Off	1	–	–	20	–
2	Off	1/3	–	–	20	–
3	Off	1/3	–	–	100	–
4	On	1	–	–	20	10.6 Myr (Case 1)
5	On	1	1073	10^4	20	10.6 Myr (Case 1)
6	On	1	1873	10^2	20	10.6 Myr (Case 1)
7	On	1/3	–	–	20	8.8 Myr (Case 2)
8	On	1/3	1073	10^4	20	8.8 Myr (Case 2)
9	On	1/3	1873	10^2	20	8.8 Myr (Case 2)
10	On	1/3	–	–	100	13.0 Myr (Case 3)

$R_{t/c}$, the ratio of tensional strength to compressional strength; T_0 and d_0/d_{min}, the parameters for the grain-size reduction (see the text); t_p, the initial age of the overriding plate; initial models for the calculation with the phase transitions.

where ρ_0 is the reference density, α the thermal expansivity, $\Delta\rho_{410}$ and $\Delta\rho_{660}$ the density contrasts associated with the 410-km and 660-km phase transitions, respectively, and Γ_{410} and Γ_{660} are phase functions associated with the 410-km and 660-km phase transitions, respectively.

The equation of energy is

$$\rho_0 c_p \left(\frac{\partial T}{\partial t} + \boldsymbol{v} \cdot \nabla T - w \frac{\alpha\, g\, (T + T_s)}{c_p} \right) - \gamma_{410} \frac{\Delta\rho_{410}\,(T + T_s)}{\rho_0} \frac{D\Gamma_{410}}{Dt} - \gamma_{660} \frac{\Delta\rho_{660}\,(T + T_s)}{\rho_0} \frac{D\Gamma_{660}}{Dt} = k\,\nabla^2 T + \sum_{i,j=1}^{2} \tau_{ij} \frac{\partial v_i}{\partial x_j} + \rho_0 H, \quad (11)$$

where T_s is the surface temperature, c_p the specific heat, k the thermal conductivity, γ_{410} and γ_{660} the Clapeyron slopes at the 410-km and 660-km phase transitions, respectively, and H is the internal heating.

The motions of the layer with the history-dependent rheology (Γ_o) and its fractured segment (Γ_F) are controlled by the equation of mass transport as

$$\frac{\partial \Gamma_l}{\partial t} + \boldsymbol{v} \cdot \nabla \Gamma_l = 0 \quad (12)$$

where l is the index for the layers replaced by o or F. The history-dependent rheology layer is represented by the position where $\Gamma_o = 1$. We determine Γ_F, which remembers the history of yielding, as follows: Before the first yielding, Γ_F is set to be 0 in the oceanic crust. When the first yielding takes place, $\Gamma_F = 1$ is imposed. We also assume that healing of the failure zone occurs at a depth of 330 km where Γ_F is reset to be 0.

We employ a finite difference method based on a control volume (CV) scheme to solve the equations. Here we use both uniform and non-uniform grids of control volumes (a dual-structure grid). The transport equations of energy (Eq. (11)) and mass (Eq. (12)) are discretized uniformly with the 2 × 2-km CVs. The total number of CVs is 3500 × 660 in the x- and z-directions. The equation of motion (Eq. (8)) is discretized non-uniformly. The regions with intense deformation (such as spreading center, subduction zone, and interior of the plate) and phase boundaries are divided into 2-km mesh spacings in each direction. Otherwise, the size of CVs varies from region to region, and is integer times larger than 2 × 2 km CVs in general. The total number of CVs is 808 × 265 in the x- and z-directions. A direct method for a symmetric band matrix (a modified Cholesky decomposition method) is applied for the equation of motion. This makes numerical calculation stable against sharp viscosity variations by more than 10^6 (Nakakuki *et al.*, 1994). In order to avoid artificial diffusion and a phase error of the equation of mass transport (Eq. (12)), the Cubic-Interpolated Pseudo-Particle (CIP) method (Takewaki *et al.*, 1985) is adopted to solve the two advection equations for Γ_o and Γ_F. The CIP method is established as a valid method to solve problems of computational fluid dynamics with sharp interfaces.

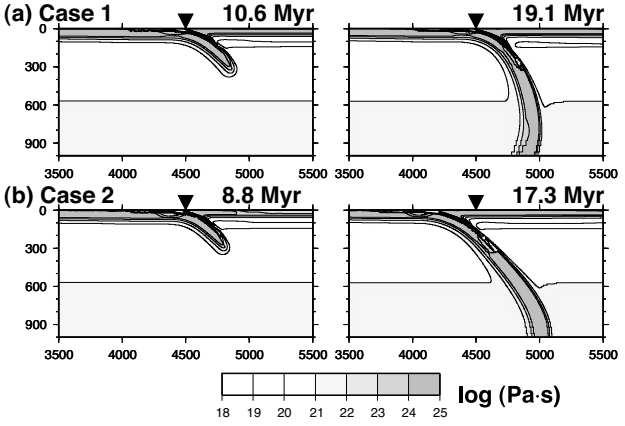

Fig. 2. Evolution of subducted slabs for the cases without phase transitions. The viscosity (Pa·s) in the logarithmic scale is shown by the contour lines and the gray scale. The contour interval is set to be 1. (a) Case 1 at 10.6 Myr and 19.1 Myr, (b) Case 2 at 8.8 Myr and 17.3 Myr. Each box shows part of the model within the width of 2000 km (horizontal) and the depth of 1000 km (vertical) surrounding the subduction zone. The initial position of the trench (x = 4500 km) is denoted by the reversed triangle.

3. Results

The cases of numerical experiments with varying parameters are summarized in Table 2. We first perform calculations without phase transitions (Cases 1, 2, and 3). In these cases a slab does not exist in the beginning. In Case 1, the slab descends almost downward because of large plate

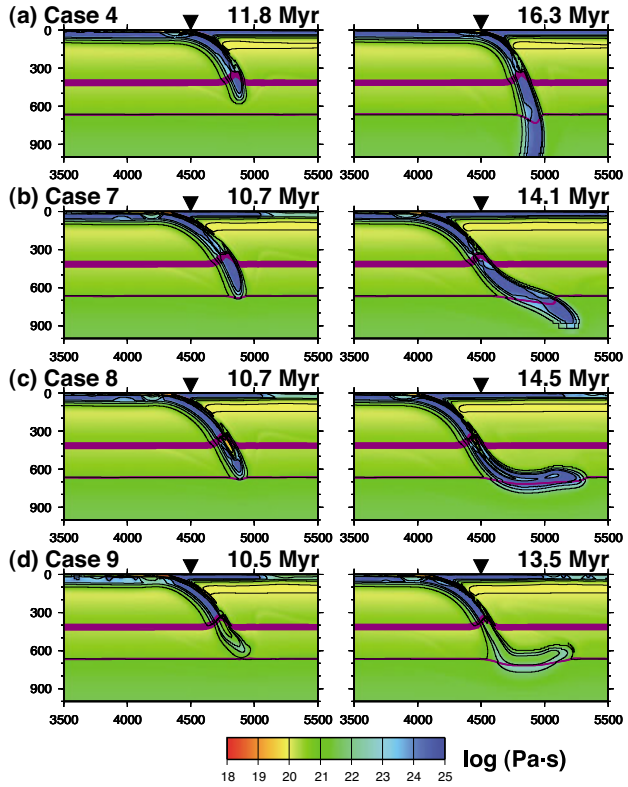

Fig. 3. Evolution of subducted slabs for the cases with phase transitions. The viscosity (Pa·s) in the logarithmic scale is shown by the contour lines and the color scale. (a) Case 4 at 11.8 Myr and 16.3 Myr, (b) Case 7 at 10.7 Myr and 14.1 Myr, (c) Case 8 at 10.7 Myr and 14.5 Myr, (d) Case 9 at 10.5 Myr and 13.5 Myr. The contour interval is the same as that of Fig. 2. The 410-km and 660-km phase boundaries are also shown by the purple lines. The initial position of the trench ($x = 4500$ km) is denoted by the reversed triangle.

bending at the trench (Fig. 2(a)). The trench is stationary because the overriding plate is not extended. In Case 2, the overriding plate with weak tensional strength is stretched by the gravitational instability of the subducting slab, and trench retreat is induced (Fig. 2(b)). The yielding occurs in a broad area of the overriding plate. At that time, only part of the overriding plate near the trench behaves as a rigid body. The trench retreat results in unbending of the subducting slab that is once bent at the trench so that the dip angle of the subducting slab becomes shallow. In Case 3, extension of the overriding plate does not occur because of the thick overriding plate of older age.

In cases with phase transitions, the calculation is started based on the results of the cases without phase transitions. We have reasons for this treatment: the slab subduction is initiated when the mantle flow produces reasonable basal drag under the plate. In cases with phase transitions, the plume-driven flow cannot induce basal drag under the plate. When the slab reaches the depth of about 350 km (Table 2), phase transitions are imposed in the model domain. At this time, the temperature change is also imposed to adjust to the latent heat generation and absorption associated with phase transitions.

Case 4 is a run with phase transitions, but without the weak tensional strength. In this case, the trench does not migrate so that the structure of the subducted slab is about the same as that in Case 1 (Fig. 3(a)). The subducted slab is almost vertical at depths deeper than the 410-km phase boundary. Positive buoyancy at the 660-km phase boundary does not prevent the slab from penetrating into the lower mantle. In Cases 5 and 6, in which grain-size reduction is introduced into the transition-zone slab, the weakened slab is deformed at the 660-km phase boundary (see Fig. A1(a) and (b)). The slab penetrates into the lower mantle, and the trench does not migrate in both the cases.

In Case 7, the weak tensional strength is introduced with phase transitions (Fig. 3(b)). When the slab interacts with the 660 km phase boundary, the positive buoyancy at the 660 km phase boundary has an effect on flattening the slab. Nevertheless, the slab penetrates into the lower mantle. The positive and negative buoyancies at the two phase transitions generate an anticlockwise torque on the slab. This enhances trench retreat so that the dip angle of the transition-zone slab becomes smaller than that in Case 2. In Case 10, the plate extension does not occur because of the thick overriding plate even if the phase transitions are introduced (see Fig. A1(c)).

In Cases 8 and 9, we also consider the effects of grain-size reduction as well as the weak tensional strength. In Case 8 the viscosity in the center of the cold slab ($<$1073 K) sharply decreases due to grain-size reduction in the transition zone (Fig. 3(c)). This makes the bending strength of the transition-zone slab weaker. A horizontally-lying slab is therefore formed above the 660-km phase boundary. In Case 9, the whole transition-zone slab becomes soft (Fig. 3(d)). In this case the slab is easily deformed and stagnates horizontally above the 660-km phase boundary. The slab rollback with extension of the overriding plate continues during the slab interaction with the 660-km phase boundary in both the cases.

Figure 4 shows the temperature and stress fields. The shallow slab shows down-dip tension (DDT) because of the negative buoyancy due to the slab density and the 410-km phase transition. On the contrary, down-dip compression (DDC) is generally observed in the slab between the 410 and 660-km phase transitions because of the positive and negative buoyancies. The detail of the stress structure changes with the style of the slab deformation depends in particular on the slab bending. In the case with the penetrating vertical slab (Case 4), the stress is the most compressive among our models (Fig. 4(a)). High compressional stress is shown above and below the 660-km phase transition. In the cases with slightly and completely stagnant slabs (Cases 7 and 8; Fig. 4(b) and (c)), both large DDT and DDC stresses are generated in the rim of the slab near the 660-km phase boundary. This reflects the slab bending. In these cases the whole layer of the slab becomes DDC in the depth range of 400 to 500 km. In Case 8, the stress in the center of the slab becomes small because of the low viscosity (Fig. 4(c)). In the case of the soft slab (Case 9), only weak stress is induced in the transition zone (Fig. 4(d)). On the other hand, large stress is generated in the center of the cold slab near the 660-km depth in Case 4 and near the 410-km depth in Case 7.

The evolution of the plate motion and the distance of the trench retreat with weak tensional strength are shown

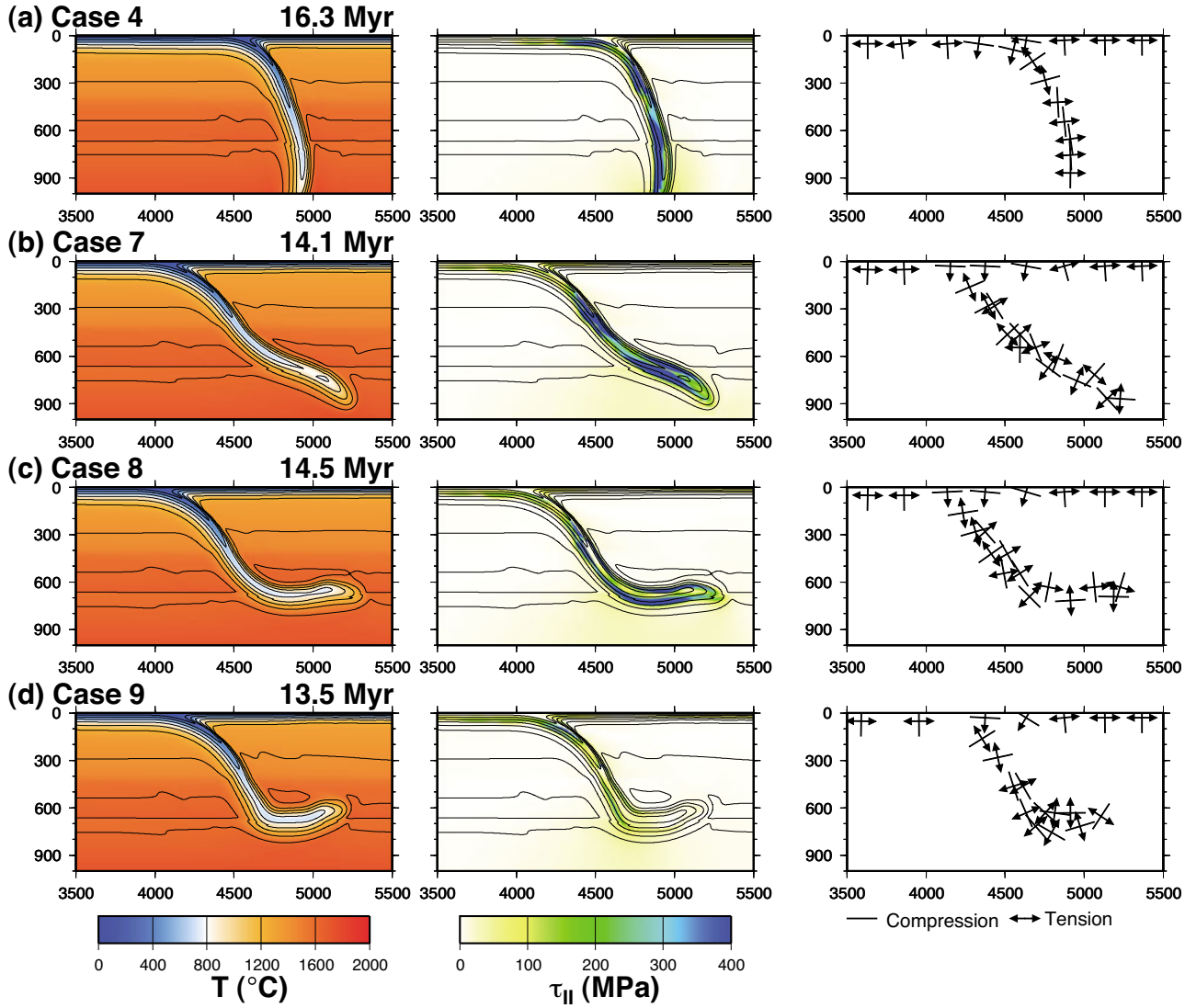

Fig. 4. Temperature (T) in °C shown by the color scale and the contour lines, second invariant of the stress tensor (τ_{II}) in MPa shown by the color scale with the temperature contour lines, and principal stress axes directions (tension and compression) for (a) Case 4 at 16.3 Myr, (b) Case 7 at 14.1 Myr, (c) Case 8 at 14.5 Myr, (d) Case 9 at 13.5 Myr. The contour interval of the temperature is 200°C.

for Cases 2, 7, 8, and 9 in Fig. 5. In Case 2 (no phase transitions), the trench migrates at 4 cm yr^{-1} and finally reaches the location 200 km left of the original point in 15 Myr. The speed of the subducting plate motion increases abruptly when the slab starts interacting with the 410-km phase boundary (Cases 7, 8, and 9) and reaches the rate of 20 cm yr^{-1}. The motion of the overriding plate block behaving as a rigid body near the trench grows simultaneously with increasing subduction rate. The motion temporally decreases after the subduction speed decreases. The slab rollback still continues (e.g., by about 350 km in 4 Myr; Case 7) with nearly constant speed after the slab starts interacting with the 660-km phase boundary.

4. Discussion and Summary

We have developed 2-D numerical subduction models in which slab rollback is produced without imposed velocity conditions on the overriding/subducting plate. We have studied the slab interaction with the mantle transition zone under the oceanic overriding plate and shown various slab deformations in the transition zone. In particular, with tensional yield strength and grain-size reduction, a horizontally-lying slab (stagnant slab) can be formed above the 660-km phase boundary. Our numerical study suggests that the feedback effects of the slab interaction with the transition zone are important in the following aspects: (1) The trench retreat is generated before the slab reaches the 660-km phase boundary and significantly influences the dip angle of the subducting slab in the transition zone; (2) the interaction of the subducted slab with the 660-km phase boundary induces the slab rollback even when the slab penetrates into the lower mantle; (3) the rollback makes the slab angle even shallower.

In our model the mechanism (1) described above enhances the effects of the positive buoyancy to prevent the slab from penetrating into the lower mantle. With the trench migration speed produced in our model ($\sim$5 cm yr^{-1} when the slab reaches the 660-km phase boundary), slab penetration into the lower mantle is prevented when the bending strength of the transition zone slab is weakened by the vis-

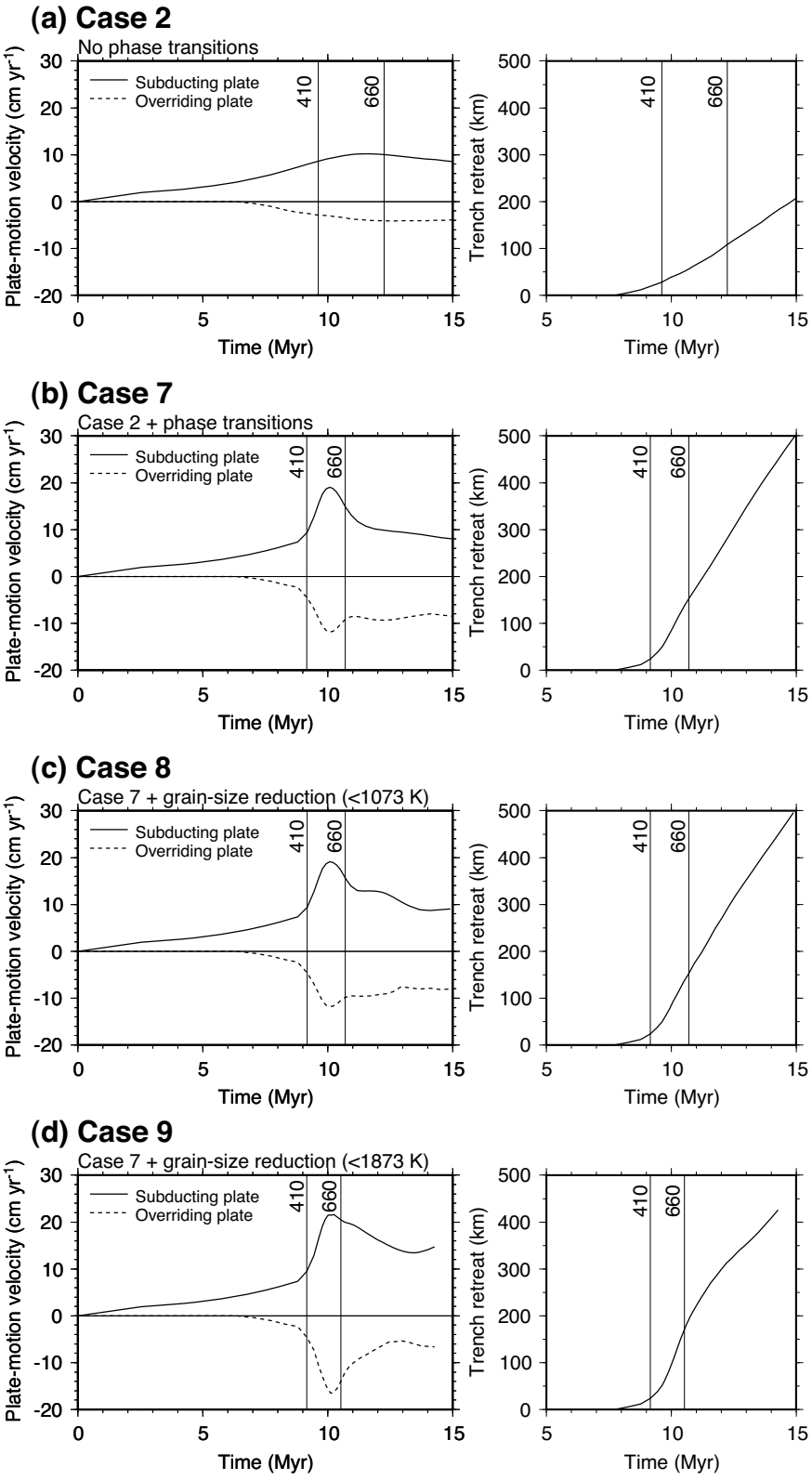

Fig. 5. Evolution of the plate-motion velocity (cm yr^{-1}) in the left diagram, and the distance (km) of the trench retreat in the right diagram for (a) Case 2, (b) Case 7, (c) Case 8, (d) Case 9. The positive value shows the speed of the subducting plate. The negative value shows the speed of the left edge of the overriding plate (i.e., trench retreat). The times when the slab reaches depths of 410 km and 660 km are indicated by the vertical lines in each figure.

cosity reduction. This is consistent with previous numerical models (Christensen, 1996; Čížková *et al.*, 2002) in which, however, the plate velocities were imposed.

The interactions of the slab with the 660-km phase boundary stimulate the slab rollback in this study. The trench migration continues for a period of over 10 Myr, a result consistent with slab rollback observed when the slab stagnates above the chemical boundary in analog experi-

ments (Kincaid and Olson, 1987; Funiciello *et al.*, 2003). Our results have also demonstrated that the combination of positive and negative buoyancies due to the phase transitions stimulates the gravitational instability of the slab and changes the slab dip angle.

We have not considered the power-law creep (e.g., Ranalli, 1987) in this study. Effects of the power-law stress dependence are equivalent to reducing the temperature and pressure dependence (Christensen, 1984). Moreover, the power-law creep is important in the shallow layer of the mantle because the activation volume (V^*) is much larger for dislocation creep than that for diffusion creep (Karato and Wu, 1993). The power-law creep is, therefore, expected to reduce the mechanical thickness of a plate and to increase viscosity gradient in the shallow mantle. These can increase the speed of the subducting plate motion and trench migration at an early stage of the subduction. The latter may enhance the effect of the 660-km phase transition to prevent slab penetration. The following mechanisms, which are not included in our model, may cause slab stagnation: the positive buoyancy due to metastable olivine (e.g., Yoshioka *et al.*, 1997; Schmeling *et al.*, 1999) and the viscous drag caused by the upwelling superplume (Gurnis *et al.*, 2000).

We compare the stress fields obtained in this study with observations. The observation shows both DDT and DDC in the shallow slab and DDC in the transition-zone slab (Isacks and Molnar, 1971). In our model the shallow portion of the slab indicates DDT. Seno and Yoshida (2004) pointed out the relationship between the shallow slab stress and the mechanism of the back-arc spreading. However, such a relationship has not been reproduced in the present study. The slab length may be important in a 3-D structure to control the stress field in the shallow slab because the plate is driven by the total force of the dense slab. The DDC of the shallow slab may indicate that the slab is pushed down by the surface plate. DDC is reproduced in the center (i.e., cold area) of the slab at around a depth of 500 km. Gurnis and Hager (1988) showed that the viscosity jump is effective to generate DDC. Our results also show that DDT and DDC coexist in the deformed and stagnant slabs around the 660-km phase boundary because of their bending. The large stress caused by the slab bending would not be important to generate deep earthquakes because the temperature in this area is higher than in the slab center.

In a soft slab (Case 9) within the transition zone, the stress level is low. This is not likely to account for the presence of deep seismicity. When the slab penetrates into the lower mantle vertically (Case 4), the direction of the principal stress axes shows DDT in the shallow slab portion (depth: 100–200 km) and DDC in the deep slab portion (depth: >300 km) being consistent with the observation in Mariana (e.g., Isacks and Molnar, 1971; Seno and Yamanaka, 1998). Slabs that penetrate the 660-km phase boundary (Cases 4 and 7) retain high stress levels in the lower mantle. This is in contrast to abrupt cessation of seismic activity below a depth of ∼700 km (e.g., Frohlich, 1989). Superplasticity (Ito and Sato, 1991; Karato *et al.*, 1995) which reduces the slab viscosity in the lower mantle may solve this discrepancy.

In our model, the extension of the overriding plate is generated by the gravitational instability of the slab and observed in a broad area of the overriding plate. If the extension occurs only locally, this would play an important role for back-arc spreading. Heuret and Lallemand (2005) summarized absolute motions of the overriding plates and the subducted slabs. The speed of the trench migration is observed between 5 and 10 cm yr^{-1} in our model. These are faster than the average trench migration speed, which is within ±5 cm yr^{-1} in most subduction zones (Heuret and Lallemand, 2005). On the other hand, the trench migration speed exceeds 10 cm yr^{-1} in some subduction zones, such as the New Hebrides arc or the Tonga-Kermadec arc (Heuret and Lallemand, 2005). In the marginal seas associated with these trenches (the North Fiji and Lau Basins), the spreading is supposed to be driven by the trench migration because the spreading rate is much faster than that of a typical mid-oceanic ridge between "subductionless" plates (Forsyth and Uyeda, 1975). In these trenches one side of the trench seems to be freely movable so that the fast slab rollback would occur. Tomography studies indicate a gentler angle in the transition zone than that in the shallower mantle in the Tonga-Kermadec subduction zone (van der Hilst, 1995). This may be explained by rollback of the slab interacting with the 660-km phase boundary. The relationship between the slab dip angle evolution and the generation of the slab stagnation is pointed out in the Izu-Bonin subduction zone (van der Hilst and Seno, 1993; Tajima and Grand, 1998).

Acknowledgments. We thank Satoru Honda for his constructive discussion and valuable comments. Comments by two anonymous reviewers helped to improve the manuscript. Most of the figures in this paper were drawn using the Generic Mapping Tools (Wessel and Smith, 1998). This study was partly supported by the Grants-in-Aid for Scientific Research No. 16075207 from the Ministry of Education, Culture, Sports, Science and Technology, Japan, and No. 16340130 from the Japan Society for the Promotion of Science.

Appendix A.

We show the viscosity of Cases 5, 6, and 10 in Fig. A1. In Cases 5 and 6 without the weak tensional strength (i.e., $R_{t/c} = 1$), the grain-size reduction is considered. In Case 10 with the weak tensional strength (i.e., $R_{t/c} = 1/3$), the overriding plate is old (i.e., 100 Ma).

Appendix B.

We used both uniform and non-uniform grids of control volumes (a dual-structure grid) in order to solve mantle convection equations. We first divide the 2-D Cartesian box into a uniform grid with the finest interval required for the numerical calculation (e.g., 2 km in the present study of subduction) for the equations of energy and mass transport. Next, we generate a non-uniform grid, in which intervals are set to be an integral proportion in size of the uniform grid, for the equation of motion. The equation of motion discretized in the non-uniform grid is described according to Kameyama (1998). The resolution of the non-uniform grid is determined depending on the expected viscosity structure. The number of the nodes is much less than that in the uniform grid so that the computation time

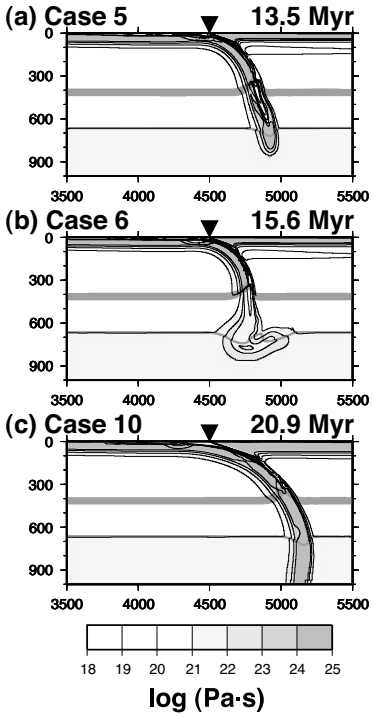

Fig. A.1. Snapshots of the subducted slabs. The viscosity (Pa·s) in the logarithmic scale is shown by the contour lines and the gray scale. (a) Case 5 at 13.5 Myr, (b) Case 6 at 15.6 Myr, (c) Case 10 at 20.9 Myr. The contour interval is the same as that of Fig. 2. The phase boundaries are also shown by the gray lines. The initial position of the trench ($x = 4500$ km) is denoted by the reversed triangle.

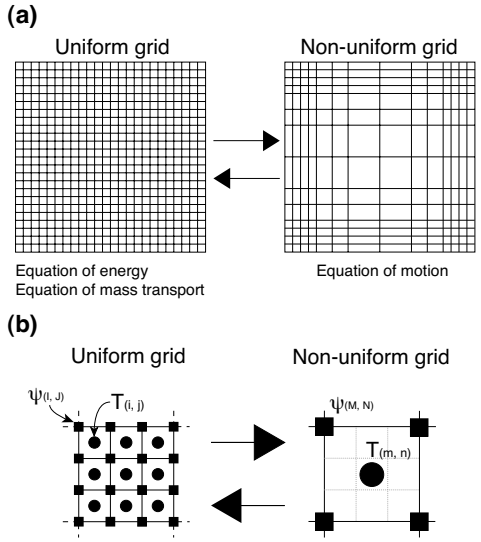

Fig. B.1. (a) Schematic view of the uniform grid (for the equations of energy and mass transport) and the non-uniform grid (for the equation of motion). (b) Control volumes and nodes for calculating the variables of the uniform grid and the non-uniform grid. The control volume of both the grids has the same structure. $\psi_{(I,J)}$ and $T_{(i,j)}$ are the stream function and the temperature in the uniform grid, respectively. $\psi_{(M,N)}$ and $T_{(m,n)}$ are the stream function and the temperature in the non-uniform grid, respectively.

is greatly reduced. Figure B1(a) illustrates the grid points in which the variables are defined. Figure B1(b) shows a control volume of the non-uniform grid which contains some control volumes of the uniform grid. The stream function (ψ) is defined at nodes of the grid. The stream function in the uniform grid is obtained by bilinear interpolation from the non-uniform grid. Because of the definition of the stream function, the conservation of mass is always proven in any interpolation scheme. The temperature (T) and the functions for the equation of mass transport are defined at the center of the control volumes in the uniform grid. These values are interpolated in the non-uniform grid taking a volumetric average of the values in the control volumes in the uniform grid.

References

Akaogi, M. and E. Ito, Refinement of enthalpy measurement of $MgSiO_3$ perovskite and negative pressure-temperature slopes for perovskite-forming reactions, *Geophys. Res. Lett.*, **20**, 1839–1842, 1993.

Akaogi, M., E. Ito, and A. Navrotsky, Olivine-modified spinel-spinel transitions in the system Mg_2SiO_4-Fe_2SiO_4: Calorimetric measurements, thermochemical calculation, and geophysical application, *J. Geophys. Res.*, **94**, 15671–15685, 1989.

Brace, W. F. and D. L. Kohlstedt, Limits on lithospheric stress imposed by laboratory experiments, *J. Geophys. Res.*, **85**, 6248–6252, 1980.

Byerlee, J. D., Friction of rocks, *Pure Appl. Geophys.*, **116**, 615–626, 1978.

Christensen, U. R., Convection with pressure- and temperature-dependent non-Newtonian rheology, *Geophys. J. R. Astron. Soc.*, **77**, 343–384, 1984.

Christensen, U. R., The influence of trench migration on slab penetration into the lower mantle, *Earth Planet. Sci. Lett.*, **140**, 27–39, 1996.

Christensen, U. R. and D. A. Yuen, The interaction of a subducting lithospheric slab with a chemical or phase boundary, *J. Geophys. Res.*, **89**, 4389–4402, 1984.

Christensen, U. R. and D. A. Yuen, Layered convection induced by phase transitions, *J. Geophys. Res.*, **90**, 10291–10300, 1985.

Čížková, H., J. van Hunen, A. P. van den Berg, and N. J. Vlaar, The influence of rheological weakening and yield stress on the interaction of slabs with the 670 km discontinuity, *Earth Planet. Sci. Lett.*, **199**, 447–457, 2002.

Dziewonski, A. M. and D. L. Anderson, Preliminary reference Earth model, *Phys. Earth Planet. Inter.*, **25**, 297–356, 1981.

Enns, A., T. W. Becker, and H. Schmeling, The dynamics of subduction and trench migration for viscosity stratification, *Geophys. J. Int.*, **160**, 761–775, 2005.

Fei, Y., J. Van Orman, J. Li, W. van Westrenen, C. Sanloup, W. Minarik, K. Hirose, T. Komabayashi, M. Walter, and K. Funakoshi, Experimentally determined postspinel transformation boundary in Mg_2SiO_4 using MgO as an internal pressure standard and its geophysical implications, *J. Geophys. Res.*, **109**, B02305, doi:10.1029/2003JB002562, 2004.

Flanagan, M. P. and P. M. Shearer, Global mapping of topography on transition zone velocity discontinuities by stacking *SS* precursors, *J. Geophys. Res.*, **103**, 2673–2692, 1998.

Forsyth, D. W. and S. Uyeda, On the relative importance of the driving forces of plate motion, *Geophys. J. R. Astron. Soc.*, **43**, 163–200, 1975.

Frohlich, C., The nature of deep-focus earthquakes, *Ann. Rev. Earth Planet. Sci.*, **17**, 227–254, 1989.

Fukao, Y., S. Widiyantoro, and M. Obayashi, Stagnant slabs in the upper and lower mantle transition region, *Rev. Geophys.*, **39**, 291–323, 2001.

Fukao, Y., M. Obayashi, H. Inoue, and M. Nenbai, Subducting slabs stagnant in the mantle transition zone, *J. Geophys. Res.*, **97**, 4809–4822, 1992.

Funiciello, F., C. Faccenna, D. Giardini, and K. Regenauer-Lieb, Dynamics of retreating slabs: 2. Insights from three-dimensional laboratory experiments, *J. Geophys. Res.*, **108**, 2207, doi:10.1029/2001JB000896, 2003.

Garfunkel, Z., C. A. Anderson, and G. Schubert, Mantle circulation and the lateral migration of subducted slabs, *J. Geophys. Res.*, **91**, 7205–7223, 1986.

Gordon, R. G., Diffuse oceanic plate boundaries: Strain rates, vertically averaged rheology, and comparisons with narrow plate boundaries and stable plate interiors, in *The History and Dynamics of Global Plate Motions*, edited by M. A. Richards, R. Gordon, and R. van der Hilst, Geophys. Monograph Series 121, pp. 143–159, Am. Geophys. Union, Washington D.C., 2000.

Gurnis, M. and B. H. Hager, Controls of the structure of subducted slabs, *Nature*, **335**, 317–321, 1988.

Gurnis, M., J. Ritsema, H.-J. van Heijst, and S. Zhong, Tonga slab deformation: The influence of a lower mantle upwelling on a slab in a young subduction zone, *Geophys. Res. Lett.*, **27**, 2373–2376, 2000.

Heuret, A. and S. Lallemand, Plate motions, slab dynamics and back-arc deformation, *Phys. Earth Planet. Inter.*, **149**, 31–51, 2005.

Isacks, B. and P. Molnar, Distribution of stresses in the descending lithosphere from a global survey of focal-mechanism solutions of mantle earthquakes, *Rev. Geophys.*, **9**, 103–174, 1971.

Ito, E. and H. Sato, Aseismicity in the lower mantle by superplasticity of the descending slab, *Nature*, **351**, 140–141, 1991.

Kameyama, M., Conditions for plate tectonics inferred from numerical experiments of mantle convection and shear zone formation, Ph.D. Thesis, University of Tokyo, 1998.

Karato, S. and P. Wu, Rheology of the upper mantle: A synthesis, *Science*, **260**, 771–778, 1993.

Karato, S., S. Zhang, and H.-R. Wenk, Superplasticity in the Earth's lower mantle: Evidence from seismic anisotropy and rock physics, *Science*, **270**, 458–461, 1995.

Katsura, T. and E. Ito, The system Mg_2SiO_4-Fe_2SiO_4 at high pressures and temperatures: Precise determination of stabilities of olivine, modified spinel, and spinel, *J. Geophys. Res.*, **94**, 15663–15670, 1989.

Katsura, T., H. Yamada, T. Shinmei, A. Kubo, S. Ono, M. Kanzaki, A. Yoneda, M. J. Walter, E. Ito, S. Urakawa, K. Funakoshi, and W. Utsumi, Post-spinel transition in Mg_2SiO_4 determined by high *P-T* in situ X-ray diffractometry, *Phys. Earth Planet. Inter.*, **136**, 11–24, 2003.

Kincaid, C. and P. Olson, An experimental study of subduction and slab migration, *J. Geophys. Res.*, **92**, 13832–13840, 1987.

Kirby, S. H., Tectonic stresses in the lithosphere: Constraints provided by the experimental deformation of rocks, *J. Geophys. Res.*, **85**, 6353–6363, 1980.

Kohlstedt, D. L., B. Evans, and S. J. Mackwell, Strength of the lithosphere: Constraints imposed by laboratory experiments, *J. Geophys. Res.*, **100**, 17587–17602, 1995.

Milne, G. A., J. X. Mitrovica, and J. L. Davis, Near-field hydro-isostasy: The implementation of a revised sea-level equation, *Geophys. J. Int.*, **139**, 464–482, 1999.

Molnar, P. and T. Atwater, Interarc spreading and Cordilleran tectonics as alternates related to the age of subducted oceanic lithosphere, *Earth Planet. Sci. Lett.*, **41**, 330–340, 1978.

Nakakuki, T., H. Sato, and H. Fujimoto, Interaction of the upwelling plume with the phase and chemical boundary at the 670 km discontinuity: Effects of temperature-dependent viscosity, *Earth Planet. Sci. Lett.*, **121**, 369–384, 1994.

Okuno, J. and M. Nakada, Effects of water load on geophysical signals due to glacial rebound and implications for mantle viscosity, *Earth Planets Space*, **53**, 1121–1135, 2001.

Ranalli, G., *Rheology of the Earth*, 366 pp., Allen and Unwin, Boston, 1987.

Riedel, M. R. and S. Karato, Grain-size evolution in subducted oceanic lithosphere associated with the olivine-spinel transformation and its effects on rheology, *Earth Planet. Sci. Lett.*, **148**, 27–43, 1997.

Rubie, D. C., The olivine→spinel transformation and the rheology of subducting lithosphere, *Nature*, **308**, 505–508, 1984.

Schmeling, H., R. Monz, and D. C. Rubie, The influence of olivine metastability on the dynamics of subduction, *Earth Planet. Sci. Lett.*, **165**, 55–66, 1999.

Scholz, C. H., *The Mechanics of Earthquakes and Faulting*, 439 pp., Cambridge University Press, New York, 1990.

Seno, T. and Y. Yamanaka, Arc stresses determined by slabs: Implications for mechanisms of back-arc spreading, *Geophys. Res. Lett.*, **25**, 3227–3230, 1998.

Seno, T. and M. Yoshida, Where and why do large shallow intraslab earthquakes occur?, *Phys. Earth Planet. Inter.*, **141**, 183–206, 2004.

Sleep, N. H., Evolution of the mode of convection within terrestrial planets, *J. Geophys. Res.*, **105**, 17563–17578, 2000.

Tajima, F. and S. P. Grand, Evidence of high velocity anomalies in the transition zone associated with southern Kurile subduction zone, *Geophys. Res. Lett.*, **22**, 3139–3142, 1995.

Tajima, F. and S. P. Grand, Variation of transition zone high-velocity anomalies and depression of 660 km discontinuity associated with subduction zones from the southern Kuriles to Izu-Bonin and Ryukyu, *J. Geophys. Res.*, **103**, 15015–15036, 1998.

Takewaki, H., A. Nishiguchi, and T. Yabe, Cubic interpolated pseudo-particle method (CIP) for solving hyperbolic-type equations, *J. Comp. Phys.*, **61**, 261–268, 1985.

Tonegawa, T., K. Hirahara, and T. Shibutani, Detailed structure of the upper mantle discontinuities around the Japan subduction zone imaged by receiver function analyses, *Earth Planets Space*, **57**, 5–14, 2005.

Turcotte, D. L. and G. Schubert, *Geodynamics: Applications of Continuum Physics to Geological Problems*, pp. 450, John Wiley and Sons, New York, 1982.

van der Hilst, R., Complex morphology of subducted lithosphere in the mantle beneath the Tonga trench, *Nature*, **374**, 154–157, 1995.

van der Hilst, R. and T. Seno, Effects of relative plate motion on the deep structure and penetration depth of slabs below the Izu-Bonin and Mariana island arcs, *Earth Planet. Sci. Lett.*, **120**, 395–407, 1993.

van der Hilst, R., R. Engdahl, W. Spakman, and G. Nolet, Tomographic imaging of subducted lithosphere below northwest Pacific island arcs, *Nature*, **353**, 37–43, 1991.

Wessel, P. and W. H. F. Smith, New, improved version of the Generic Mapping Tools released, *EOS Trans. Am. Geophys. Union*, **79**, 579, 1998.

Yamazaki, D., T. Inoue, M. Okamoto, and T. Irifune, Grain growth kinetics of ringwoodite and its implication for rheology of the subducting slab, *Earth Planet. Sci. Lett.*, **236**, 871–881, 2005.

Yoshioka, S., R. Daessler, and D. A. Yuen, Stress fields associated with metastable phase transitions in descending slabs and deep-focus earthquakes, *Phys. Earth Planet. Inter.*, **104**, 345–361, 1997.

Zhong, S. and M. Gurnis, Mantle convection with plates and mobile, faulted plate margins, *Science*, **267**, 838–843, 1995.

M. Tagawa (e-mail: tagawa@geol.sci.hiroshima-u.ac.jp), T. Nakakuki, and F. Tajima